Journal of Electronics, Electromedical Engineering, and Medical Informatics
Homepage: jeeemi.org; Vol. 8, No. 2, April 2026, pp: 730-750 e-ISSN: 2656-8632

RESEARCH ARTICLE OPEN ACCESS

Robust Brain Tumor MRI Classification Through MobileNetV3 Deep Feature Fusion and Principal Component Analysis Enhanced AdaBoost Learning

Ahmed Aizaldeen Abdullah[1], Hadeel Safaa Hussein[2], and Laith Ali Abdul Rahaim[3]

[1] Department of Electromechanical Techniques, Baqubah Technical College, Middle Technical University, Baghdad, Iraq
[2] College of Engineering, Al-Iraqia University, Baghdad, Iraq
[3] Department of Electrical Engineering, University of Babylon, Babil, Iraq

Corresponding author: Ahmed Aizaldeen Abdullah (e-mail: handsome.eng82@mtu.edu.iq), **Author(s) Email**: Hadeel Safaa Hussein (e-mail: hadeel.s.hussein@aliraqia.edu.iq), Laith Ali Abdul Rahaim (e-mail: drlaithanzy@uobabylon.edu.iq)

Abstract **Among the most serious neurological diseases are brain tumors, which pose a challenge to early detection through MRI due to low contrast, tissue heterogeneity, and high-dimensional deep features that make it difficult for traditional classification models to be effective. This study proposes a robust and computationally efficient multi-class classification framework capable of distinguishing four tumor types: glioma, meningioma, pituitary tumor, and no tumor. The primary contributions are: (1) the development of a hybrid feature-learning pipeline that introduces a hybrid feature-learning framework in which a one-level 2D Discrete Wavelet Transform (2D-DWT) is employed as a multi-resolution preprocessing step to enhance MRI slices prior to deep feature extraction using MobileNetV3; (2) the application of Principal Component Analysis (PCA) to compress a 1,024-dimensional deep-feature vector into only 20 principal components, achieving a 99.96% reduction in dimensionality; (3) the use of an optimized AdaBoost ensemble specifically adapted for low-dimensional inputs; and (4) achieving performance that surpasses several published approaches evaluated on the same benchmark dataset. The proposed workflow includes cropping, normalization, and CLAHE enhancement, followed by 2D-DWT to extract LL, LH, HL, and HH sub-band information. The wavelet-refined MRI slices are processed by MobileNetV3 to implicitly encode spectral–textural information into deep semantic representations, which are subsequently reduced using PCA and classified by AdaBoost. Experiments conducted on a public Kaggle brain MRI dataset comprising 7023 images show that MobileNetV3 combined with 2D-DWT achieves an accuracy of 99.56%. When enhanced with PCA and AdaBoost, the full framework attains 99.94% accuracy, 99.95% precision, 99.96% recall, 99.94% F1-score, and 100% AUC, demonstrating remarkable tumor discrimination performance. In summary, the proposed PCA–AdaBoost hybrid framework offers a highly accurate, lightweight, and clinically promising solution for automated brain tumor MRI classification.**

Keywords **Brain Tumor, Principal Component Analysis (PCA), Discrete Wavelet Transform (2D-DWT), Deep Learning, MobileNetV3, Adaptive Boosting (AdaBoost)**

I. Introduction

One of the most serious neurological diseases is brain tumors. There are multiple pathological types of brain tumors, but for the purposes of the study, tumor classification included 3 major types (gliomas, meningiomas, and pituitary) and one minor: healthy (non-cancerous) brain MRI scans were also utilized, so there was complete data available for all 4 classifications. Despite being the best way to visualize the brain, MRI is limited by factors such as low contrast, scanner differences, tumor diversity, and similar patterns of texture, all of which reduce diagnostic accuracy [1]. Traditional machine-learning methods based on handcrafted features (such as GLCM or LBP) often struggle to achieve robustness and generalization comparable to modern deep learning architectures, particularly in complex and heterogeneous brain MRI classification tasks, which is why deep learning methods are being developed. Recent advancements in deep CNN architectures demonstrate superior results in classifying brain tumor MRIs than traditional MRI classification methods. The hybrid CNN-LSTM model uses multi-scale spatial properties to achieve greater than 98% accuracy when evaluated on been

Manuscript received 11 January 2026; Revised 20 March 2026; Accepted 15 April 2026; Available online 24 April 2026
Digital Object Identifier (**DOI**): https://doi.org/10.35882/jeeemi.v8i2.1462

shown to achieve greater than 99% accuracy when identifying tumors [3]. The two architecture types require an extraordinary amount of computational resources (CPU/GPU), training time, and extensive parameter optimization to perform optimally. Deep learning models often yield high classification accuracy; however, they require a tremendous amount of computational resources. Typically, deep learning architectures such as large Convolutional Neural Network (CNN) ensembles or Transformer architectures have tens of millions of parameters and require enormous floating-point operations per second (FLOPS) in order to execute the computations involved in training. Increased resource usage during training, increased resource utilization, and increased time for processing are apparent across most medical imaging domains on low computational infrastructure. Lightweight architectures remain in high demand, as they produce a high level of performance while minimizing the size and cost associated with the models.

U-Net++, vision transformers, and deep encoder-decoder ensembles are effective at delivering high levels of accuracy when diagnosing images, but their high complexity & computational demands make them unsuitable for use in high-volume urgent care settings where speed is critical [4]. Other hybrid models that use combinations of ecological descriptors and deep learning results (e.g., GoogLeNet-ELM combined with GLCM/LBP) provide performance consistent with these other model categories; however, they require extensive preprocessing pipelines [5]. Moreover, most CNN-only methods lack spectral-domain analysis, resulting in potential loss of valuable frequency-domain information [6]. Several recent studies have aimed to improve four-class tumor classification. Ensemble models that combine InceptionV3 and Xception achieved 98.3%–98.5% accuracy but rely on a single dataset and omit spectral features [7]. Another ensemble fusing VGG16, ResNet50, and AlexNet yielded 99.16% accuracy but required running three heavy CNNs simultaneously, limiting deployability [8]. Res-BRNet achieved 98.22% accuracy on three tumor categories but was optimized for a specific dataset and is sensitive to domain shift across MRI scanners [9].

Other frameworks use multiple CNNs for binary, five-class, and tumor-grading tasks, achieving up to 99.53% accuracy but at the cost of architectural complexity and lack of explainability [10]. Hybrid deep-texture systems combining CE-EEN-B0 and ResGANet with LBP and HOG reached 99.11% accuracy yet required complex preprocessing, genetic programming, and multi-stage fusion [11]. Comparative studies using LBP, Gabor, DWT, FFT, and CNN classifiers reported 98.9% accuracy but relied mainly on texture-based descriptors, lacking semantic deep features [12]. Transfer-learning studies involving SqueezeNet, InceptionV3, and MobileNetV2 achieved 99.2% accuracy, but were evaluated on limited datasets [13]. Multi-wavelet–VGG16 fusion models obtained 96.43% accuracy across six datasets but did not fully integrate frequency-domain features within the classifier [14]. CNN–LSTM hybrids achieved 99.1% accuracy but introduced unnecessary temporal modeling for static MRI data [15].

A review of the literature indicates three main limitations in current approaches: Most deep learning methodologies ignore spectral-domain information and multi-resolution wavelet features; furthermore, deep CNNs produce many redundant feature vectors, which increase the computational burden of these algorithms. Many high-performing methodologies also incorporate either complex ensembles or transformer-based models, creating barriers to their use in real-time or resource-constrained clinical settings. Due to these limitations, there is a need for a hybrid lightweight framework that integrates spectral, textural, and semantic features into a compact and discriminative representation of the input data.

Although CNNs are good at learning spatial representations, they mainly learn in the spatial domain; therefore, they may not be able to adequately identify the frequency-based characteristics found in medical imaging. Most brain tumor MRIs have small intensity changes, irregularly shaped tumors, and a mixture of texture types. All of these features can be better represented in the frequency spectrum of the image. The decomposition cycle using wavelet-based methods divides the image into multiple frequency levels, allowing both global structures and fine textures to be identified. This ability of the spectral domain descriptors to provide additional information to improve tumor discrimination will assist in enhancing image processing using deep CNN features. Using squeeze-and-excitation attention and improved residual blocks, MobileNetV3 strikes an ideal ratio between efficiency and accuracy. When comparing performance on an efficiency basis with the original EfficientNet-B0, MobileNetV3 performs equally but with less computing power, making it suitable for real-time clinical use.

MobileNetV3 was chosen for the backbone because of its good compromise between computation efficiency and representation capability. Depth-wise separable convolutions decouple standard convolution into separately processing spatial filters and channel-level projections, significantly reducing the computational cost of the convolution operation. In addition, MobileNetV3 has inverted residual blocks and linear bottlenecks that allow efficient reuse of features while maintaining information flow between different layers of the model. Lastly, squeeze-and-excite attention mechanisms are incorporated into the

Manuscript received 11 January 2026; Revised 20 March 2026; Accepted 15 April 2026; Available online 24 April 2026
Digital Object Identifier (**DOI**): https://doi.org/10.35882/jeeemi.v8i2.1462

MobileNetV3 design to further improve the calibration of features derived from the channel dimension. Therefore, the MobileNetV3 architecture has been designed to achieve comparable accuracy with a fraction of the data required by most traditional CNN architectures, making it a great fit for both medical imaging and real-time clinical settings.

The researchers in this study have developed a hybrid lightweight feature-learning framework using mixed-resolution information, deep semantic representations, and more compact dimensionality-reduced descriptor outputs in a unified processing pipeline. They have combined an initial application of a one-level 2D Discrete Wavelet Transform (2D-DWT), which produces LL, LH, HL, and HH sub-bands that are valuable for capturing critical spatial-spectral variations that have been typically lost or ignored using traditional Convolutional Neural Networks (CNNs), with processing the 2D-DWT-enhanced MRI slices with MobileNetV3 to generate feature-rich, low computational cost semantic features. To eliminate excessive redundancy of features, the authors reduced the 1024-dimensional vector to 20 principal components (PCs) using Principal Component Analysis (PCA), while maintaining 99.96% of the dimensionality of the feature vector and preserving most of the discriminative information of the feature vector. Finally, the authors employed an AdaBoost-based ensemble classifier to increase the diversity of decision boundaries to address potential issues of class imbalance and improve classifier robustness. The integrated framework captures both local textural and global structural patterns in MRI images while maintaining operational efficiency. The authors illustrate that their framework has potential for use in clinical deployment.

The main objective of this research is to develop an accurate, robust, and computationally efficient classification framework for four-class brain-tumor MRI images by integrating 2D-DWT spectral descriptors, MobileNetV3 deep features, PCA dimensionality reduction, and an AdaBoost ensemble classifier. This article presents the following advances on prior work: (i) a hybrid system that employs 2D-DWT–MobileNetV3 techniques to extract spectral and semantic features; (ii) a new system to accomplish effective feature compression via Principal Component Analysis (PCA), resulting in a 99.96% reduction in dimensionality; (iii) an enhanced AdaBoost classifier with both improved accuracy and lower computational expense; and (iv) a lightweight, clinically deployable MRI diagnostic pipeline for four classes that demonstrates superior performance compared to existing approaches.

Section II of this manuscript details the methodology, including data preprocessing, wavelet decomposition, deep feature extraction, PCA-based dimensionality reduction, and AdaBoost classification. Section III details the experimental setup, including the dataset description and evaluation metrics. Section IV reports the obtained results and compares the performance with recent state-of-the-art studies. Section V provides analytical discussions. Finally, Section VI summarizes the conclusions and highlights potential future research directions.

II. Method

In order to increase convolutional neural networks' representational capacity, a deep learning framework has been developed that combines the use of one-level two-dimensional Discrete Wavelet Transform (2D-DWT) with MobileNetV3 Architecture and PCA (Principal Component Analysis). PCA is performed to reduce the dimensionality of features while preserving those features that provide optimal discrimination capabilities to form a compact and effective feature space. The blocks of the proposed method are shown in Fig. 1. The ultimate outcome of the proposed approach is to enable the classification of the four brain tumors found within the Kaggle dataset of MRI images. Three stages were incorporated in creating the proposed processing system. Stage 1 preprocessing of the input MRI image includes increasing contrast, decreasing noise, and extracting multiple resolution frequency information from (2D-DWT), helping the deep learning model learn relevant structure and texture features. In the second stage, deep features are extracted using MobileNetV3 and then fused with wavelet-domain features to form a powerful hybrid representation. This stage also includes model architecture selection, training, evaluation, baseline comparison, and performance assessment. In the final stage, PCA is applied to reduce redundant features, and the resulting compact feature vector is fed into the AdaBoost classifier to perform four-class tumor categorization with high accuracy and computational efficiency.

A. Datasets Collection and Class Distribution

This study employs the publicly available Brain Tumor MRI dataset obtained from Kaggle (https: // www. Kaggle. com / datasets / masoudnickparvar / brain-tumor-mri-dataset), which is widely used for benchmarking four-class brain-tumor classification systems. The dataset comprises MRI slices categorized into two broad classes (tumor and non-tumor), where tumor images are further divided into three clinically relevant subtypes: pituitary tumors, meningioma tumors, and glioma tumors. The 1st Kaggle release consists of 2000 MRI images, which include 1000 non-tumor and 1000 tumor images. The tumor subset consists of 300 pituitary, 400

Manuscript received 11 January 2026; Revised 20 March 2026; Accepted 15 April 2026; Available online 24 April 2026
Digital Object Identifier (**DOI**): https://doi.org/10.35882/jeeemi.v8i2.1462

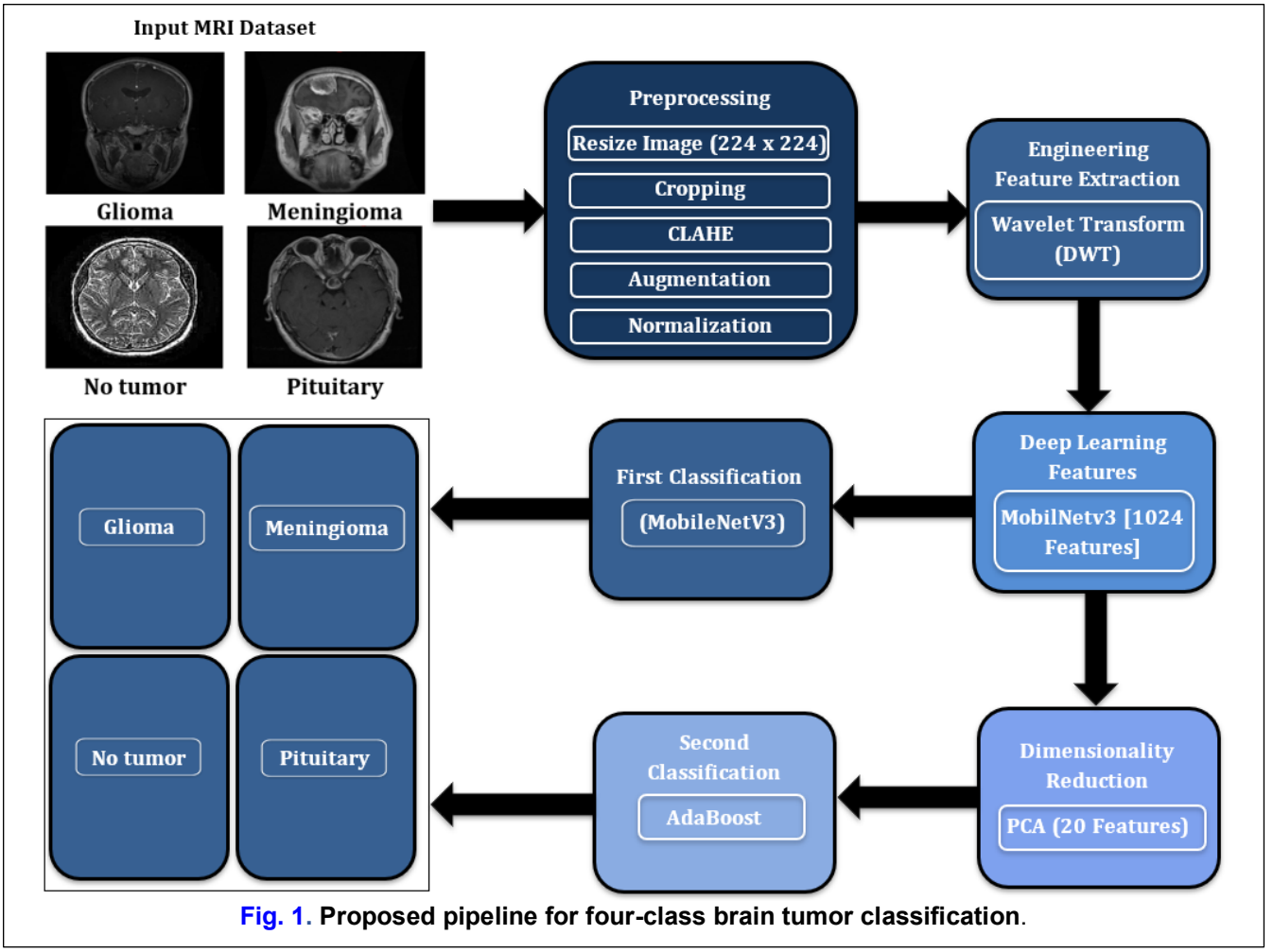

Fig. 1. Proposed pipeline for four-class brain tumor classification.

meningioma, and 300 glioma MRI scans. To enhance model generalizability and allow for better assessment of model performance on a wider range of sample data distributions, a more extensively defined version of the dataset with 7023 images was used in this research. The extended dataset was then subdivided into 5712 images for training and 1311 images for testing purposes.

The extended dataset was divided into 5,712 training and 1,311 testing images using stratified sampling strategy. Stratification was applied to preserve the original class distribution across both subsets, ensuring balanced representation of all four diagnostic categories. The purpose of this stratification approach was to reduce sampling bias, eliminate class balance (especially for minority classes), and provide a reliable assessment of how well the model generalizes.

B. pre-processing

All MRI images have been pre-processed using a pipeline to ensure consistent, high-quality input to the classification framework. The preprocessing pipeline comprises three stages. First, image cropping removes unwanted backgrounds. Second, intensity normalization makes pixel values consistent across all scans. Finally, the use of Contrast Limited Adaptive Histogram Equalization (CLAHE) for contrast enhancement will improve the quality of each individual scan by emphasizing the edge of the tumor while providing images with stable characteristics for wavelet decomposition and deep feature extraction later on in the pipeline. Finally, data augmentation was applied to increase variability, reduce overfitting, and improve the model's generalization.

1. Resize Image and Cropping

This dataset comprises multiple brain tumor MRI images taken from multiple native resolutions (512×512 to 1024×1024 pixels). In order to provide the same input format for training with MobileNetV3 and to make all the images compatible with each other, all of the images were resized to 224×224 pixels for this study. The images were resized in this manner to be subsequently cropped during data set preparation. All of the cropped images retain their original aspect ratio while having the non-anatomical background areas cropped away so that the study model has the capability of focusing on only the anatomical areas that

Manuscript received 11 January 2026; Revised 20 March 2026; Accepted 15 April 2026; Available online 24 April 2026
Digital Object Identifier (**DOI**): https://doi.org/10.35882/jeeemi.v8i2.1462

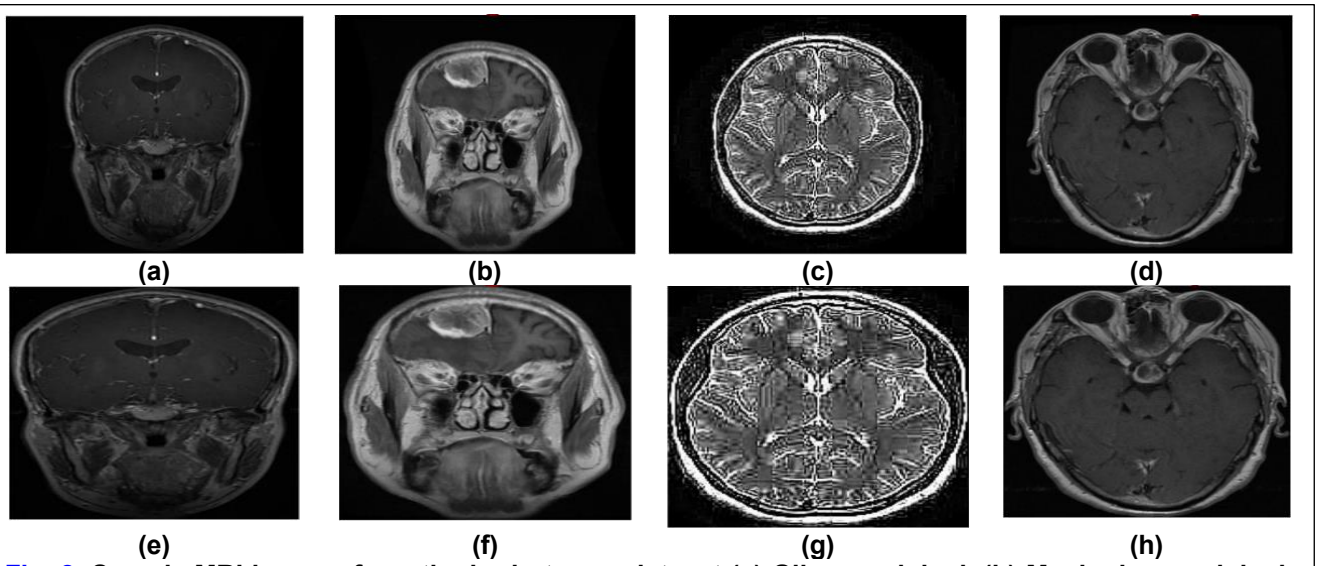

Fig. 2. Sample MRI images from the brain-tumor dataset (a) Glioma original, (b) Meningioma original, (c) No tumor original, (d) Pituitary original, (e) Glioma cropped, (f) Meningioma cropped, (g) No tumor cropped, (h) Pituitary cropped.

contain the tumors, as demonstrated in Fig. 2. With these practices, this study achieves two significant advantages by reducing the amount of computation needed to generate the model (by removing the background areas of each image) and by making more effective use of the features of the anatomical structures of interest in the development of the model.

2. Image Enhancement

After cropping and normalization, image enhancement is applied to improve visual clarity and strengthen feature discrimination. CLAHE is used to increase local contrast, reduce illumination inconsistencies, and reveal subtle tumor boundaries that may not be visible in raw MRI scans(Fig. 3). The CLAHE parameters were set as follows: clipLimit = 2.0 and tileGridSize = (8 × 8). These values were empirically selected to enhance local contrast while preventing noise amplification in homogeneous regions. This enhancement improves fine structural details and contributes to better classification performance. A mathematical description of the CLAHE process is provided in [16], [17], [18], [19], where the input image is divided into contextual regions (tiles) as defined in Eq. (1) [16]. Histogram equalization is then applied independently to each tile to enhance local contrast.

$$T = \frac{N \times N}{n \times n} \quad (1)$$

Tiles in the images $n \times n$ pixels. The clip limit, an important parameter, is used to create the necessary histograms in Contrast Limited Adaptive Histogram Equalization (CLAHE) to control how much contrast enhancement is applied locally to prevent over-amplification of noise and artifacts. CL, as delineated in Eq. (2) [17].

$$C_L = N_{CL} \times N_{AVG} \quad (2)$$

Where, N_{CL} stands for normalization contrast limit, and N_{AVG} is the image's average pixel count.

The percentage of N_{AVG} is calculated using Eq. (3) [18].

$$N_{AVG} = \frac{N_x \times N_y}{N_g} \quad (3)$$

The number of grey scales, pixel dimensions on the x-axis, and pixel dimensions on the y-axis inside the tile are indicated by the N_x, N_g and N_y parameters. Eq. (4) is used to calculate the average values of the quantity of clip pixels [19].

$$N_{CP} = \frac{N \sum C_L}{N_{gr}} \quad (4)$$

where, C_L denotes as cut pixels, while $N \sum C_L$ represented the entire amount of C_L.Some pixels stay after the Ncp is spread between the changed levels of grey.

3. Augmentation and Normalization

An extensive data augmentation strategy was applied during the training phase to improve model generalization and reduce the risk of overfitting. Data augmentation was applied to provide realistic variations to MRI slices while maintaining the tumor characteristics. To increase representation of tumor characteristics and minimize the effects of acquisition and orientation differences, data augmentation was used that included random horizontal and vertical flipping, rotation (±15°), scaling with a range of (0.9, 1.1), mild shearing, and increased brightness. Finally, all MRI images had their intensities normalized so that

Manuscript received 11 January 2026; Revised 20 March 2026; Accepted 15 April 2026; Available online 24 April 2026
Digital Object Identifier (**DOI**): https://doi.org/10.35882/jeeemi.v8i2.1462

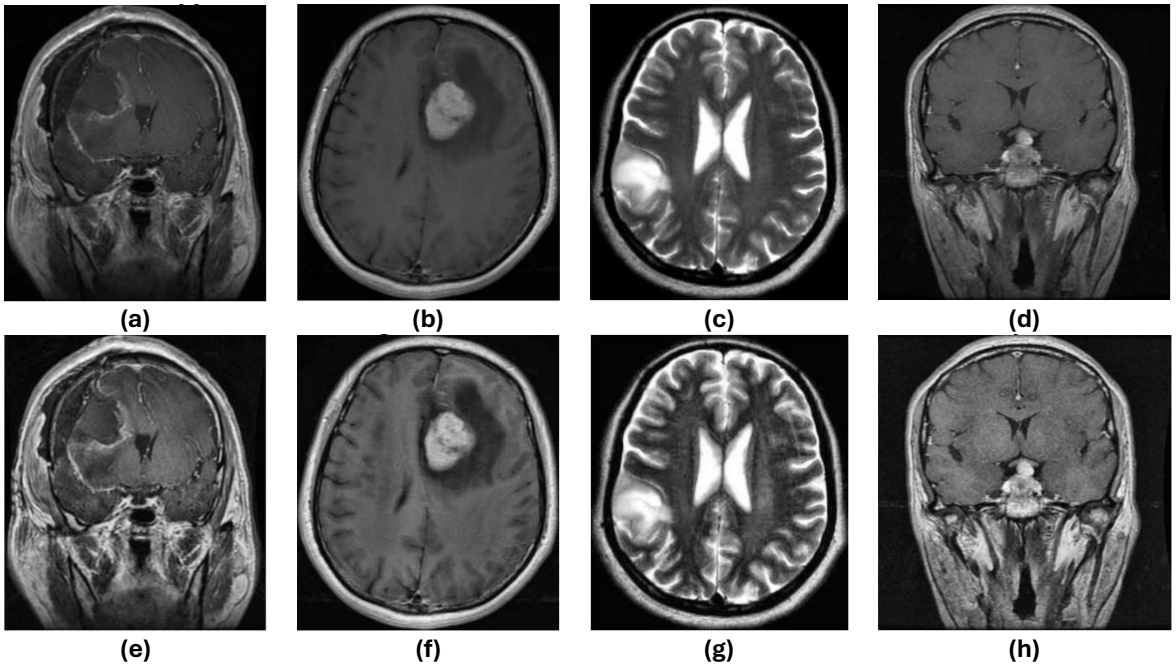

Fig. 3. CLAHE enhancement results for four brain-tumor MRI images (a) Glioma cropped, (b) Meningioma cropped, (c) No tumor cropped I, (d) Pituitary cropped, (e) Glioma (CLAHE), (f) Meningioma (CLAHE), (g) No tumor (CLAHE), (h) Pituitary (CLAHE).

pixel intensity was consistent for all scan images, regardless of which scanner/protocol created them.

Normalizing pixel intensities to a common scale also accelerates training convergence and stabilizes gradient updates. In this study, min–max normalization was applied to map pixel intensity values into the range [0, 1], as defined by Eq. (5) [20], [21], [22]:

$$I\_norm = (I - I\_min) / (I\_max - I\_min) \quad (5)$$

Normalized pixel value I_norm equals the original pixel value and has been scaled from the minimum pixel value I_min to the maximum pixel value I_max of the image to range from 0 to 1. This is done to provide consistent values for perception and to enhance image usability for execution by mathematical algorithms. This normalization step reduces inter-scan intensity variability and enhances feature discriminability, providing a robust and consistent input for subsequent 2D-DWT decomposition and deep feature extraction.

C. Engineering Feature Extraction

Feature extraction allows the classification process to focus on only the most significant feature set, as opposed to all available features, which has the effect of reducing the amount of data to be used for the classification process and, in turn, allows for easier interpretation. By identifying the most relevant features for a given classification, an information source becomes much easier to manage while retaining the most relevant properties of the original data source. One method used to accomplish this is to apply a one-level Discrete Wavelet Transform (2D-DWT) to MRI images of brain tumors, which provides both spectral and texture descriptors at multiple levels of resolution. The low sub-band frequencies contain high-level representations of coarse anatomy, while the high sub-band frequencies focus on subtle structural differences. When combining the features derived from the wavelets, the overall dimension of the data is reduced, allowing for more efficient processing of the data set. Furthermore, it will provide an efficient means of classifying a brain tumor into one of four categories, with minimal computational requirements due to the significant reduction in the size of the data set that needs to be processed.

D. Wavelet Transform

Mathematical transformations can be used on medical images to extract structural and frequency-based information that is not clear in the original format of the image. The Fourier transform and the wavelet transform are the two main families of mathematical transformations. The Wavelet Transform (WT) represents a mathematical structure used to break up an image into small, localized basis functions (also referred to as small waves). The Discrete Wavelet Transform (2D-DWT) breaks down an image through a two-step process involving convolution and down-sampling the image [23]. A two-dimensional discrete wavelet transform (2D-DWT) was performed with a one level of decomposition using the Daubechies-4 (db4) mother wavelet. The db4 wavelet was chosen for its

Manuscript received 11 January 2026; Revised 20 March 2026; Accepted 15 April 2026; Available online 24 April 2026
Digital Object Identifier (**DOI**): https://doi.org/10.35882/jeeemi.v8i2.1462

good time-frequency localization and the validity of its smooth base functions in medical texture analysis [24]. A single-level decomposition was purposely chosen to maintain the spatial resolution while capturing the important approximation (low-frequency) and detail (high-frequency) components with a minimum of decomposition. Multi-level decompositions may create redundant representations and increase computational complexity, while the single-level decomposition provides an optimal compromise between enhancing features and efficiency.

In the (2D-DWT) formulation, low-pass and high-pass filters are denoted by $h(n)$ and $g(n)$, associated with their respective impulse responses $h(n)$ and $g(n)$. After performing the filtering operation, a decimation step occurs (indicated by a down-arrow), where the sampling frequency is reduced by 2x. The process of splitting and filtering to down-sample can be done recursively on the approximated (scaling) coefficients, which produces a multi-scale hierarchical representation of the image. During the first stage of decomposition, the input signal $X[n]$ has its low-frequency (approximate) and high-frequency (detail) components separated, providing the initial scaling and wavelet coefficient data. In the second stage, the Approximation Sub-band is again decomposed into a Low-Pass and a High-Pass Sub-band, thereby generating a Multi-Resolution Structure at a deeper level. The decomposition process is hierarchical and continues until the desired level of detail has been achieved. As a result, the Discrete Wavelet Transform has found many uses within a variety of fields related to Image Processing because of its capability to provide representations both of the Coarse Structure of an Image and of the Fine Texture of the Image. In creating the (2D-DWT), two Primary Functions are used to define the (2D-DWT): the Scaling Function and the Wavelet Function. The scaling function represents the low-pass component of the signal and is mathematically defined through the refinement relations shown in Eq. (6) and Eq. (7) [22]:

$$low = \sum_n x[n].l[2k-n] \quad (6)$$

$$high = \sum_n 2x[n].H[2k-n]n \quad (7)$$

The low-frequency part of the signal Eq. (6) is found by multiplying the data from the original signal ($x[n]$) with a scaling function ($l[2k-n]$) and summing over every possible value of n. The high-frequency part of the original signal ($x[n]$), which includes finer details from the original signal, can be calculated using the wavelet function ($H[2k-n]$), as shown in Eq. (7).

The scientific definition of the first phase of the discrete wavelet transform (2D-DWT) is provided in (5) and (6). The wavelet transform can be used for a two-dimensional (2D) signal decomposition and separates the 2D signal into approximation coefficients, which represent low-frequency components, and detail coefficients, which represent high-frequency components. A 2D separable wavelet transform can be viewed as performing two consecutive 1D wavelet transforms. The first 1D transform is performed horizontally, row by row, producing intermediate row-wise coefficients. Subsequently, a second 1D transform is applied vertically to the intermediate row-wise coefficients, creating the four sub-bands: LL, LH, HL, and HH.

The 2D-DWT computation has two main algorithm groups: the separable method and the non-separable method. The Separable Method filter and down-sampling steps are performed independently for each dimension using the same filter. All of the rows are processed first, followed by all of the columns that result from the row processing in the Separable Method. The Non-Separable Method works a little differently; it processes the image using both the horizontal and vertical dimensions simultaneously within a single phase rather than separating the computation into a Row Phase and a Column Phase. In general, Non-Separable Method algorithms can minimize the amount of computation that must be performed while increasing the numerical efficiency of the algorithm, but these algorithms are generally more challenging to implement and lesswidely used as the Separable Method algorithms due to their increased complexity [25]. The Decomposition Framework creates the foundation for a multi-resolution analysis, making it possible to extract important features regarding structural or textural characteristics from brain-tumor MRIs.

Mathematically, let I(x, y) denote the input MRI image. The one-level 2D-DWT is computed by applying separable one-dimensional low-pass and high-pass filters along the row and column directions, followed by down-sampling by a factor of two. Let H0 and H1 represent the low-pass and high-pass filters applied along the rows, and G0 and G1 denote the corresponding filters applied along the columns. The resulting sub-band coefficients are defined in Eq. (8), Eq. (9), Eq. (10), and Eq. (11) [25]:

$$\mathrm{LL(i,j)} = \left((\mathrm{I} * \mathrm{H_0})_{\{\mathrm{row}\}} * \mathrm{G_0}\right)_{\{\mathrm{col}\}} \quad (8)$$

$$\mathrm{LH(i,j)} = \left((\mathrm{I} * \mathrm{H_0})_{\{\mathrm{row}\}} * \mathrm{G_1}\right)_{\{\mathrm{col}\}} \quad (9)$$

$$\mathrm{HL(i,j)} = \left((\mathrm{I} * \mathrm{H_1})_{\{\mathrm{row}\}} * \mathrm{G_0}\right)_{\{\mathrm{col}\}} \quad (10)$$

$$HH(i,j) = \left((I * H_1)_{\{row\}} * G_1\right)_{\{col\}} \quad (11)$$

where * denotes the convolution operation. The LL sub-band captures the low-frequency approximation information, while the LH, HL, and HH sub-bands

Manuscript received 11 January 2026; Revised 20 March 2026; Accepted 15 April 2026; Available online 24 April 2026
Digital Object Identifier (**DOI**): https://doi.org/10.35882/jeeemi.v8i2.1462

represent vertical, horizontal, and diagonal detail components, respectively. Sub-sampling after filtering reduces the spatial resolution by 50% in each dimension at the first decomposition level. The 1-level 2-dimensional discrete wavelet transform (2D-DWT) produces four sub-band representations by recursively decomposing the LL (low frequency) band into several layers. Thus, the LL band is at the top layer, with increasingly fine detail running down through the lower levels. This study utilizes only the first (coarse) level of wavelet decomposition to extract the most informative textural and frequency information from MRI images. All MRI slices was used before carrying out a wavelet transformation, and the db4 (Daubechies-4) wavelet function was selected due to its ability to capture fine details present in medical images. Four 2D-DWT sub-bands are produced from this process: LL (approximation coefficients), LH (vertical), HL (horizontal), and HH (diagonal). Collectively, the LL, LH, HL, and HH sub-bands represent both the high-level global structure and the low-level detailed texture of these tumor regions. Wavelet decomposition inherently decrease spatial resolution; therefore, given that the input image was resized to 224 × 224 pixels, it is found that the sub-band representation of the LL contains only 112 × 112 pixels at the first level. Dimensionality reduction can create a compact representation of denoised data while isolating only the most salient image features for feature extraction purposes. Wavelet-based feature extraction dramatically reduces the input data's dimensionality while preserving important tumor-specific descriptors, which have improved the performance of the downstream AdaBoost classifier. Fig. 4 illustrates the effect of the entire preprocessing pipeline, including cropping and CLAHE enhancement, followed by a single-level two-dimensional discrete wavelet transform (2D-DWT) decomposition. This produced a number of sub-bands that allow for efficient extraction of discriminative features used for multi-class brain tumor classification in a multi-resolution manner.

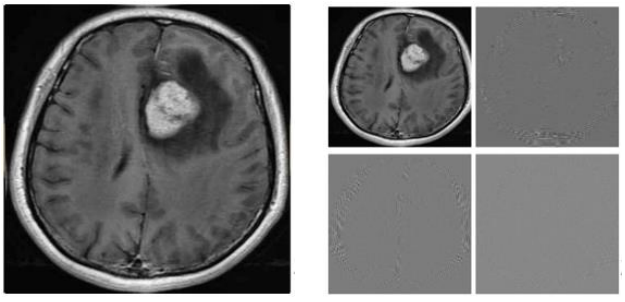

(a) (b)

Fig. 4. One-level 2D-DWT decomposition of Brain Tumor MRI (LL, LH, HL, HH) (a) Original Image (224,224,3), (b) One-Level 2D-DWT (112,112).

The image produced from 2D-DWT pre-processing is shown in Fig. 4. Each MRI image is broken down into four separate sub-bands (LL, LH, HL, HH). The LL component contains information about global anatomy, whereas the other three components give us information about edges and textural characteristics. This additional spectral data should assist in identifying any tumor-related patterns before extracting deep features.

E. MobileNet

It is easy to see by the name that MobileNet is a product of Google, where they have leveraged their expertise and work to create a very viable lightweight (compared to other architectures) and fast neural network architecture as a means of creating an accelerated version of deep learning methods that work for the mobile device industry. MobileNet has become a very popular model within the deep-learning community and has proven to be very durable and versatile; therefore, the popularity of MobileNet models on mobile devices such as smartphones and embedded systems such as IoT devices has created a wide array of mobile computing and real-time computer vision capabilities. As a result, MobileNet has become the most widely used choice in the marketplace for edge computing solutions or real-time computer vision solutions because of its ability to achieve a very good size-to-computational efficiency ratio and lightweight design. By creating MobileNet pre-trained models, the ability to create many different types of deep-learning applications with limited processing power (in many cases) on a mobile device has become much more achievable. Developers use transfer learning extensively fto develop efficient deep-learning applications for edge/mobility and as the primary source for the continued evolution of AI technologies at the edge based on computer vision [26], [27].

Additionally, MobileNet pre-trained models for feature extraction are being developed, offering smaller model sizes while maintaining extremely high computational efficiency. To reduce the computational burden associated with standard convolutions, MobileNet employs depth-wise separable convolutions, which are essentially a combination of two types of 2D convolutions (depth-wise and point-wise). In addition to separating the computation of the spatial component from the channel component, depth-wise separable convolutions allow you to use a width multiplier to adjust the width of a MobileNet, thereby providing more flexibility regarding the trade-off between model performance and size. Furthermore, the resolution multiplier adjusts the resolution of the input image so that a reduced-resolution image produces a smaller and faster inference model. Many MobileNet variants also use inverted residual blocks,

Manuscript received 11 January 2026; Revised 20 March 2026; Accepted 15 April 2026; Available online 24 April 2026
Digital Object Identifier (**DOI**): https://doi.org/10.35882/jeeemi.v8i2.1462

which can reduce computational cost while preserving their structural integrity and representation strength.

MobileNet is a pre-trained model that is becoming increasingly popular within transfer learning frameworks due to its ability to be quickly and easily adapted for use with smaller task-specific datasets to address a wide variety of applications in computer vision. MobileNets have been trained on extensive data sets, including ImageNet; therefore, they can be effectively fine-tuned for different tasks by making slight adjustments to the parameters of the pre-trained model. In this study, the MobileNetV3-Large model acts as a deep feature extractor for features that represent the high-level semantics of the brain MRI slices. Transfer learning using pre-trained weights from the ImageNet dataset was incorporated by initializing the model with those weights. The classification layer was removed from the model to allow it to function solely as a feature extractor, and deep features were extracted from the global average pooling layer located immediately before the classification layer, producing a 1,024-dimensional deep-feature vector. During training, the convolutional layers of MobileNetV3 were fine-tuned to adapt the learned representations to the brain tumor MRI domain. The extracted deep features were subsequently forwarded to the PCA-based dimensionality reduction and AdaBoost classification stages. This configuration corresponds to the MobileNetV3 backbone summarized in Table 1.

The main reason for MobileNet's efficiency is because it uses depth-wise separable convolutions (DSC); instead of performing the filtering and mixing of channels in a single step as done with regular convolutions, DSC splits this into two distinct steps: a depth-wise convolution where each filter is applied separately to each input channel and a point-wise (1×1) convolution that merges all of the filtered input channels into one output channel by multiplying the output of each channel by a matrix. By separating filtering and channel mixing, rather than performing them simultaneously, DSC significantly reduces computational costs and the size of MobileNets. In a standard convolutional layer, an input feature map **F** of size DF × DF × N is transformed into an output feature map **G** of size DG× DG × M. DF and DG are determined using a convolution kernel **K** of size DK ×DK × N× M, where DK represents the spatial dimensions of the convolutional kernel. This expression illustrates the high computational cost associated with standard convolution, as detailed in Eq. (12) [28]. MobileNet alleviates through depth-wise separable factorization.

$$G_{k,l,m} = \sum_{i,j,n} K_{i,j,m,n} \cdot F_{k+i-1,l+j-1,n} \quad (12)$$

where $G_{k,l,m}$ = output feature map after applying convolution, $K_{i,j,m,n}$ = convolution kernel to filter the input feature map, and $F_{k+i-1,l+j-1,n}$ = input feature map at the given position. The indices i, j, and n represent the positions for the kernel and input feature map during the convolution process.

There is a direct multiplicative relationship between the computational cost of a convolutional layer and several key variables: the kernel size (D_K), the spatial dimension of the feature map (D_F), and the number of input and output channels (N and M, respectively). MobileNets reformulate the convolution operation to explicitly express the relationship between the variables. MobileNets use depth-wise separable convolutions to independently relate the number of output channels to the kernel size, thus allowing spatial filtering and channel mixing to occur independently of each other. As such, the decoupling of these two processes reduces the computational cost of performing both tasks while maintaining the model's representational strength.

A depth-wise separable convolution (DSC) consists of two parts: first, a depth-wise convolution, and then, a pointwise convolution. In the depth-wise convolution, each filter is applied to each channel separately so that each filter filters each channel spatially and independently from one another. The outputs from all the depth-wise filters get aggregated using a pointwise convolution (also referred to as a 1×1 convolution) to mix the different output channels. MobileNet architectures use Batch Normalization and ReLU Nonlinearity layers between both steps to make them more stable and to improve the overall learning process. The mathematical expression of a depth-wise convolution, assuming the use of a single filter for each input channel, is given in Eq. (13) [28].

$$\hat{G}_{k,l,n} = \sum_{i,j} \hat{K}_{i,j,n} \cdot F_{k+i-1,l+j-1,n} \quad (13)$$

$\hat{K}$ denotes the depth-wise convolution kernel applied to the m^{th} channel of the input feature map *F*, producing the corresponding m^{th} channel in the output feature map $\hat{G}$. The computational cost of a Depth-wise Separable Convolution (DSC) is obtained by summing the individual costs of its two components, depth-wise convolution, and pointwise convolution, as formulated in Eq. (14) [28].

$$DSC_{COst} = D_K \times D_K \times N \times D_F D_F + N \times M \times D_F \times D_F \quad (14)$$

where DSC_{COst} represents the total computational costs of depth-separable convolution. The values for D and K are defined as the spatial dimensions of a convolution kernel. The value of N is the number of input (filters) channels, and M is the number of output (filters) channels. The values of D and F are defined as the spatial dimensions of the feature map. The computational cost is reduced by reformulating the convolution operation as a two-phase process, filtering followed by channel combining, which allows the cost

Manuscript received 11 January 2026; Revised 20 March 2026; Accepted 15 April 2026; Available online 24 April 2026
Digital Object Identifier (**DOI**): https://doi.org/10.35882/jeeemi.v8i2.1462

of DSC to be expressed as a ratio relative to the cost of a standard convolution, as shown in Eq. (15) [28].

$$\frac{D_K \times D_K \times N \times D_F \times D_F + N \times M \times D_F \times D_F}{D_K \times D_K \times N \times M \times D_F \times D_F} = \frac{1}{N} + \frac{1}{D_K^2} \quad (15)$$

The width multiplier is a key hyperparameter introduced to further reduce the computational cost of convolutional neural networks and to construct lightweight MobileNet architectures. In MobileNet, this parameter uniformly scales the number of input and output channels in each layer, such that the channels become αN and αM,respectively. By decreasing the channel dimensions, the width multiplier substantially lowers both the computational cost of depth-wise separable convolutions (DSC) and the total number of trainable parameters, often by a factor of four. Its value typically ranges between 0 and 1, allowing controlled model compression without severely degrading performance. The computational cost of applying the width multiplier to DSC is mathematically expressed in Eq. (16) [28]:

$$DSC_{COst} = D_K \times D_K \times \alpha N \times D_F \times D_F + \alpha N \times \alpha M \times D_F \times D_F \quad (16)$$

Eq. (16) represents the cost of depth-wise separable convolution (DSC) multiplied by a dimension multiplier (width multiplier). The multiplier for the number of input/output channels has the effect of reducing the cost associated with computing the convolution. The number of input channels is represented as N, and the number of output channels is M. The convolution's spatial dimensions are represented as DK, and the spatial dimensions of the feature map as DF.

MobilityNet's hyperparameter, resolution multiplier ρ, provides a way for MobileNet to lower the image resolution/size before passing the image through the MobileNet architecture. As a result, at each layer of MobileNet, there will be lower-level feature representations, and hence less computation required to process an input through MobileNet. When lowering an input image's spatial (width and height) dimensions, then all feature representations will be reduced by a proportionate size across the entire MobileNet architecture, resulting in much faster inferencing times and decreased computational complexity compared to using higher-resolution images. The resolution multiplier has a mathematical effect when applied to the depth-wise separable convolution in MobileNet, as shown in Eq. (17) [28].

$$DSC_{COst} = D_K \times D_K \times \alpha N \times \rho D_F \times \rho D_F + \alpha N \times \alpha M \times \rho D_F \times \rho D_F \quad (17)$$

The model's architecture is based on the MobileNet, which uses 3×3 depth-wise separable convolutional layers and reduces computational costs significantly compared to traditional convolutional layers with little loss in accuracy. MobileNet has been utilized to extract deep-level features from processed images of brain tumors in the Kaggle database. PCA has been used to compress the lower-resolution representation of the feature maps obtained from MobileNet, and the compressed feature maps have been processed by an AdaBoost classifier, which compensates for the fact that MobileNet produces feature maps that are much smaller than those produced using traditional methods while providing excellent prediction capabilities.

By preprocessing through a 2D-DWT, multi-resolution representations provide richer spatial information for networks. The LL band captures the course architectural structure, while the LH, HL, and HH bands accentuate directional edges and finer textures associated with areas known or suspected to have tumors. Through MobileNetV3, convolutional filters in mobile networks apply different weights to structural and spectral-textural patterns, allowing the recognition of more discriminative characteristics and thereby improving classification success rates.

1. Proposed Model Layers Architecture

The MobileNetV3 model architectural configuration is summarized in Table 1 with details of each layer's architecture, kernel sizes, tensor size, and all other operational parameters. Each of the 3 types of neural networks (convolutional, pooling, and transformation networks) has a stride of 2 that assists in spatially progressive down-sampling, maximizing computational efficiency as well. To assist with managing overfitting and variability, all fully connected layers utilize a dropout rate of 0.25. The dimensions of the tensors decrease as the depth of the network increases (while each tensor's dimension can typically be halved at each depth), which allows for compressing the spatial representation while still retaining a semantically rich representation. Towards the end of the MobileNet path (the upper half) of the network, a dense bottleneck layer is implemented through a fully connected layer that consists of 512 units, utilizing a ReLU activation for providing high-level abstraction and nonlinear transformation prior to classification. For multi-class brain tumor classification, the last layer contains a SoftMax activated unit that generates probability distributions for the four diagnostic categories of pituitary tumor, meningioma tumor, glioma tumor, and

Table 1. MobileNetV3 model layer attributes.

Layer (type)	Output Shape
MobileNetV3	(None, None, None,1024)
(GlobalAveragePooling2D)	(None, 1024)
dropout (Dropout)	(None, 1024)
dense (Dense)	(None, 512)
(Batch Normalization)	(None, 64)
dense_1 (Dense)	(4)

Manuscript received 11 January 2026; Revised 20 March 2026; Accepted 15 April 2026; Available online 24 April 2026
Digital Object Identifier (**DOI**): https://doi.org/10.35882/jeeemi.v8i2.1462

no tumor. The network will be trained using the Adam optimizer, a widely accepted and robust means of optimizing deep neural networks that offers reliable and efficient convergence during the training process.

2. Proposed Model training and hyperparameters

Directional optimization of the selected architecture's weights was performed using stochastic gradient descent (SGD) on an initial training dataset that had been pre-processed. As a result, deep learning can develop high-quality representations from brain tumor MRI images that are highly discriminative and correctly classify into diagnostic types. Continuous monitoring of tmodel performance throughout the different training epochs occurred by way of evaluation metrics, such as accuracy and loss. The hyperparameters were adjusted and optimized until they reached their peak in performance, as presented in Table 2. The proposed

Table 2. Hyperparameters for Our Suggested Model.

hyperparameter	Value
epochs	300
dropout	0.25
batch size	64
optimizer	Adam
learning rate	0.00001
loss	Binary Cross Entropy
activation	SoftMax

model is intended to perform a multiclass classification. The network was trained simultaneously using all four categories of brain tumor: pituitary, meningioma, glioma, and no tumor. This allowed the network to identify both common and distinct features associated with each tumor type. A joint training approach provides greater robustness with respect to the overall performance of all tumor types since it enables the model to better understand how to differentiate between tumor types. Performance meant to keep providing stable, precise, repeatable results. Due to the nature of a clinical setting, both under- and overfitting may create significant clinical complications for responsible clinicians taking care of patients. To develop a highly reliable model for use in medical diagnosis, datasets were carefully constructed to allow adequate representation of each tumor type, and the training process included extensive optimization and hyperparameter tuning to produce an equally robust and accurate classification of each tumor category.

F. Principal Component Analysis (PCA)

Principal Component Analysis (PCA) was employed to reduce the dimensionality of the deep feature vectors extracted from MobileNetV3 while preserving the most discriminative information [29]. Let $X \in \mathbb{R}^{\{N\times D\}}$ denote the deep feature matrix, where N represents the number of MRI samples and D = 1024 is the original feature dimensionality obtained from the global average pooling layer of MobileNetV3.

First, mean centering is applied to normalize the feature matrix by subtracting the mean vector μ from each feature vector, as defined in Eq. (18) and Eq. (19) [30]:

$$X_{centered} = X - \mu \quad (18)$$

where:

$$\mu = \left(\frac{1}{N}\right)\sum_{i=1}^{N} X_i \quad (19)$$

Next, the covariance matrix $\Sigma \in \mathbb{R}^{\{D\times D\}}$ is computed by Eq. (20) [30]:

$$\Sigma = \left(\frac{1}{(N-1)}\right) X_{centered}^{T} X_{centered} \quad (20)$$

Eigen-decomposition is then performed on the covariance matrix to obtain a set of eigenvalues $\{\lambda_k\}$ and corresponding eigenvectors $\{v_k\}$, such that by Eq. (21) [30]:

$$\Sigma\, v_k = \lambda_k v_k \quad (21)$$

The eigenvectors are sorted in descending order according to their associated eigenvalues. The top K = 20 eigenvectors corresponding to the largest eigenvalues are selected to construct the projection matrix given in Eq. (22) [30]:

$$W = \left[v_1, v_2, \ldots, v_{\{20\}}\right] \quad (22)$$

Finally, the original feature matrix is projected onto the reduced PCA subspace to obtain the transformed feature representation as defined in Eq. (23) [30]:

$$X_{reduced} = X_{centered} W \quad (23)$$

where $X_{reduced} \in \mathbb{R}^{\{N\times 20\}}$ represents the compact feature matrix used as input to the AdaBoost classifier. This PCA-based dimensionality reduction achieves 99.96% reduction in feature dimensionality while maintaining strong discriminative capability. The PCA analysis provides the cumulative explained variance shown in Fig. 5. The first 20 principal components account for most of the total variance of the deep feature space; therefore, the proposed framework was used with the first 20 components.

G. Adaptive Boosting Algorithm (AdaBoost) for Classification

Designed in 1995 by Freund and Schapire, AdaBoost is one of the most well-known and accepted machine learning algorithms today because it provides a way to combine many weaker classifiers into a single strong classifier. Because it was the first successful implementation of boosting, AdaBoost uses weak classifiers that are usually single-split decision trees (sometimes called Decision Trees due to their shallow nature). AdaBoost.M1 is the most used version of AdaBoost and is primarily used in binary classification

Manuscript received 11 January 2026; Revised 20 March 2026; Accepted 15 April 2026; Available online 24 April 2026
Digital Object Identifier (**DOI**): https://doi.org/10.35882/jeeemi.v8i2.1462

tasks. During training, AdaBoost constructs a set of weak classifiers in an iterative way, adjusting the weights assigned to the training samples after every iteration. The weights assigned to the misclassified examples are increased, while the weights assigned to the correctly classified examples are decreased. This gives subsequent classifiers greater emphasis on the harder-to-classify training samples than on the easier-to-classify ones, progressively improving the model's predictive ability and overall performance [31].

To ensure optimal performance on the PCA-reduced low-dimensional feature space, the AdaBoost classifier was optimized through systematic hyperparameter tuning. The optimization process focused on key parameters that directly influence ensemble behavior, including the number of weak learners (n_estimators) and the learning rate. A grid-search-based strategy was employed on the training set to evaluate multiple parameter combinations, with classification accuracy and validation stability used as the primary selection criteria. The best set of training conditions utilized 150 weak classifiers and a learning rate of 0.8, producing the most optimal balance between truthfulness of prediction through improving classification accuracy and refining decision boundaries while providing the least possible computational cost. Shallow decision trees (decision stumps) were selected as base learners, as they are well-suited for boosting on compact, low-dimensional PCA feature representations. In order to be able to use AdaBoost in a low-dimensional feature space generated by PCA, the parameters of the classifier were optimized by making use of a grid search to find the optimal number of weak classifiers and the optimal learning rate. Because decision stumps (shallow decision trees) perform well in a compact representation of features, they were selected as the base learners. The reduction in the dimensions of the features allowed AdaBoost to focus its learning on the most discriminative components of the data, thereby improving the stability of the final classifier and refining the decision boundaries. The final configuration consisted of 150 weak classifiers and a learning rate of 0.8, providing an appropriate balance between accuracy and computational efficiency. This optimization strategy ensures that AdaBoost effectively exploits the reduced PCA feature space by preventing underfitting at small ensemble sizes and overfitting at excessive boosting depths.

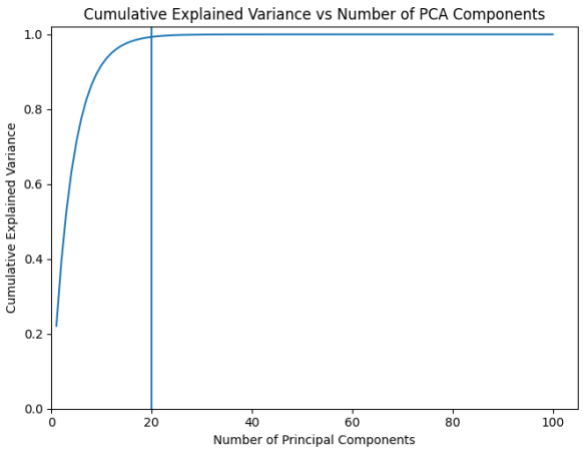

Fig. 5. Cumulative explained variance versus number of principal components.

The AdaBoost classifier was designed to function optimally within the PCA-featured space. The reduced size of the deep feature vectors allows the algorithm to target those dimensions that hold the greatest informational value, thus letting each weak learner more clearly differentiate between very complex class boundaries. By giving increased weights to misclassified samples, the boosting process allows future classifiers to continue adjusting the decision boundary until it is clearly defined. Therefore, the structural nature of AdaBoost makes it a very effective algorithm for the situation where compact feature representations resulting from PCA are used in conjunction with AdaBoost.

In this study, AdaBoost is employed as the final classifier on top of the PCA-compressed low-dimensional feature space in order to refine decision boundaries and improve class separability. AdaBoost is an iterative ensemble learning algorithm that constructs a strong classifier by linearly combining multiple weak learners, each trained to focus on samples that were misclassified in previous iterations. Let $\{(x_i, y_i)\}_{\{i=1\}}^{N}$ denote the training dataset, where $x_i \in R^{\{20\}}$ represents the PCA-reduced feature vector and $y_i \in \{-1, +1\}$ is the corresponding class label. Initially, equal weights are assigned to all training samples by Eq. (24) [32], [33]:

$$w_i^{\{(1)\}} = \frac{1}{N} \quad (24)$$

At iteration t, a weak learner $h_{t(x)}$ (implemented as a decision stump) is trained using the weighted training samples. The weighted classification error ε_t of the weak learner is computed as Eq. (25) [32], [33]:

$$\varepsilon_t = \sum_{\{i=1\}}^{N} w_i^{\{(t)\} I\left(h_{t(x_i)} \neq y_i\right)} \quad (25)$$

where $I(\cdot)$ is the indicator function. Based on this error, the confidence (weight) of the weak learner is calculated as Eq. (26) [32], [33]:

$$\alpha_t = \frac{1}{2} \ln\left(\frac{(1-\varepsilon_t)}{\varepsilon_t}\right) \quad (26)$$

Where α_t is the confidence (weight) of the weak learner at iteration t, calculated based on the classification error ε_t. The sample weights are then updated to emphasize misclassified samples by Eq. (27) [32], [33]:

Manuscript received 11 January 2026; Revised 20 March 2026; Accepted 15 April 2026; Available online 24 April 2026
Digital Object Identifier (**DOI**): https://doi.org/10.35882/jeeemi.v8i2.1462

$$w_i^{\{(t+1)\}} = w_i^{\{(t)\}\exp}\left(-\alpha_t y_i h_{t(x_i)}\right) \quad (27)$$

where $w_i^{\{(t+1)\}}$ is the updated weight of the i-th sample after the t-th boosting iteration. After updating, the weights are normalized so that $\sum_{\{i=1\}}^{N} w_i^{\{(t+1)\}} = 1$. This iterative process is repeated for T boosting rounds. The final strong classifier $\mathrm{H(x)}$ is obtained as a weighted sum of the weak learners by Eq. (28) [32], [33]:

$$H(x) = sign\left(\sum_{\{t=1\}}^{T} \alpha_t h_{t(x)}\right) \quad (28)$$

Where H(x) is the final strong classifier after T boosting rounds. It is a weighted sum of all the weak learners.

Algorithm 1: AdaBoost.M1

Input:
Training data S = $\{(\boldsymbol{x_1}, \boldsymbol{y_1}), \ldots, (\boldsymbol{x_2}, \boldsymbol{y_2}), \ldots, (\boldsymbol{x_m}, \boldsymbol{y_m})\}$,
Base learner $\boldsymbol{h(x)(decision\ stump)}$,
Number of iterations T.
Procedure:
Initialize the weight $\boldsymbol{w_i^1 = \frac{1}{N},\ for\ i = 1, 2, \ldots, N}$
For t = 1, …, T:
1) Train the weak classifier $\boldsymbol{h_t(x)}$ using the weighted samples $\{\boldsymbol{w_i^t}\}$.
2) Compute the classifier weight
$\boldsymbol{\varepsilon_t = \sum_{\{i=1\}}^{N} w_i^t I\left(h_{t(x_i)} \neq y_i\right)}$
3) Compute the weak learner weight:
$\boldsymbol{\alpha_t = \frac{1}{2}\ln\left(\frac{(1-\varepsilon_t)}{\varepsilon_t}\right)}$
4) Update sample weights
$\boldsymbol{w_i^{t+1} = w_i^t \exp\left(-\alpha_t y_i h_{t(x_i)}\right)}$
5) Normalize the weights so that
$\boldsymbol{\sum_{\{i=1\}}^{N} w_i^{t+1} = 1}$
End for
Output:
Final strong classifier:

$$\boldsymbol{H(x) = sign\left(\sum_{\{t=1\}}^{T} \alpha_t h_{t(x)}\right)}$$

The sign function indicates the final predicted class (positive or negative). By adaptively focusing on difficult-to-classify samples, AdaBoost effectively refines the decision boundaries in the reduced PCA feature space. This makes the classifier particularly well-suited for low-dimensional representations, where it improves class separability and enhances overall classification accuracy.

The introduction to the AdaBoost Algorithm is contained in Algorithm 1 [34]. This algorithm is generally easy to implement and does not usually require a lot of hyperparameter adjustments. In addition, the flexibility of AdaBoost allows users to choose any type of model for their base learners, and by using the method of boosting, practitioners may improve the model being used for the task. However, one major drawback of AdaBoost is that its iterative reweighting strategy creates a greater sensitivity to noise and/or outliers in the data, which may result in overfitting the model in certain instances.

An AdaBoost classifier is used on top of the PCA-compressed feature space as the final decision model, using a total of 150 weak learners (n_estimators=150), a learning rate of 0.8, and a fixed random state of 42. Typically, weak learners are shallow decision trees, and AdaBoost will increase the weights of the misclassified training samples and create a strong ensemble generated from the weak base classifiers. This approach allows the AdaBoost classifier to learn from the reduced 20-dimensional feature vectors while using the compactness and discriminative ability of the PCA-transformed deep features to construct a more robust classification stage with better decision boundary refinement, increased generalization performance, and lower complexity in both training and inference compared to directly training from the original high-dimensional deep feature space.

H. Mathematical Modeling

Define $D_{\{i=1\}}^{N} = \{(I_I, y_I)\}$, where $\mathrm{I_i} \in \mathrm{R^{\{H\times W\times 3\}}}$, $\mathrm{y_i} \in \{1,2,3,4\}$ (glioma, meningioma, pituitary, and no tumors). Eq. (29), Eq. (30), Eq. (31), Eq. (32), Eq. (33), Eq. (34), and Eq. (35) represent the complete and formal representation of the method given in this paper. The framework developed here can also be expressed as a composite mapping of these equations.

$$\hat{\mathrm{y}}_\mathrm{i} = \mathrm{C}\left(\mathrm{P}\left(\mathrm{F}\left(\mathrm{W}\left(\mathrm{T}(\mathrm{I_i})\right)\right)\right)\right) \quad (29)$$

where $\hat{\mathrm{y}}_\mathrm{i}$ is the predicted label for sample i. It represents the classification output after applying all the steps in the framework. $T(\cdot)$ denotes preprocessing, $W(\cdot)$ stands for 2D-DWT decomposition, $F(\cdot)$ is a MobileNetV3 deep feature extractor, $P(\cdot)$ is a PCA dimensional reduction process, and, lastly, $C(\cdot)$ is an AdaBoost classifier.

1. Preprocessing Model: The preprocessing term $T(\cdot)$ encompasses cropping, contrast-limited adaptive histogram equalization (CLAHE), and intensity normalization. The normalized image formula is defined as follows:

$$\mathrm{I_i^n} = \frac{(\mathrm{I_i} - \mathrm{I_{min}})}{(\mathrm{I_{max}} - \mathrm{I_{min}})} \quad (30)$$

By normalizing the original sample's image $\mathrm{I_i^n}$, we can create a normalized version of that image ($\mathrm{I_i}$). The lowest pixel value for the original sample image will be called I_{min}, and its highest pixel value will be called I_{max}. The result will establish a stabilized input domain for decomposing via wavelets.

Manuscript received 11 January 2026; Revised 20 March 2026; Accepted 15 April 2026; Available online 24 April 2026
Digital Object Identifier (**DOI**): https://doi.org/10.35882/jeeemi.v8i2.1462

2. Representation in the Wavelet Domain: Assume that an image is already preprocessed; thus, let us denote I_i^n as an example. A one-level 2D-DWT using a separable filter and downsampling will yield four subbands as follows:

$$W(I_i^n) = \{LL_i, LH_i, HL_i, HH_i\} \quad (31)$$

Amongst the four wavelet representation bands, LL_i contains the low-frequency anatomical structure, and the remaining three bands (i.e., $LH_i, HL_i, \text{and } HH_i$) emphasize vertical, horizontal, and diagonal details, which contribute to tumor boundary detection and irregularities in texture.

3. Implicit spectral-semantic fusion through deep feature extraction with a framework that performs this function in MobileNetV3 without having to merge concatenated features. We will represent MobileNetV3's feature extractor as Φ(·; θ). The resulting deep feature vector will be a hybrid representation:

$$z_i = \Phi(W(I_i^n); \theta) \in R^D, \; D = 1024 \quad (32)$$

The z_i feature vector represents a hybrid representation, which is due to the fact that the wavelet operation modifies the input spatial-frequency characteristics of the image before the convolutional learning begins.

4. The PCA algorithm reduces the dimensionality of the overall deep features, $Z = [z_1^T, \ldots, z_N^T]^T \in R^{\{N \times D\}}$. PCA projects Z onto a low-dimensional subspace defined by the dimension K (here K=20):

$$x_i = (z_i - \mu)W \in R^K \quad (33)$$

where μ=mean feature vector and $W \in R^{\{D \times K\}}$ are the top K eigenvectors of the covariance matrix. The low-dimensional discriminative feature space corresponds to the resulting x_i,, which will be used for classifying new data.

5. The multi-class model for AdaBoost aggregates the results of T training classifiers $\{h_{t(x)}\}_{\{t=1\}}^T\}$, and outputs a strong classifier:

$$H(x) = \text{argmax}_{\{c \in \{1,\ldots,4\}\}} \sum_{\{t=1\}}^T \alpha_t \cdot I(h_{t(x)} = c) \quad (34)$$

The AdaBoost classifier produces a binary output $H(x)$ from an input variable (x). The individual classifiers produced by the weak classifiers at each iteration t are assigned weights (α)t. I(·) is an indicator function that returns 1 if the condition is satisfied and 0 otherwise. $h_{t(x)}$ is the weak classifier at iteration t, and c represents the class label (1 of 4 possible tumor types) in this case. Here, α_t is the weight associated with classifier t, and I(·) is the indicator function. Sample weight w_i^t for classifier t gets updated based on which samples were misclassified from a previous iteration. Thus, for sample i at iteration t+1:

$$w_i^{t+1} = \frac{\left[w_i^t \cdot \exp\left(\alpha_t \cdot I\left(h_{t(x_i)} \neq y_i\right)\right)\right]}{\sum_{\{j=1\}}^N \left[w_j^t \cdot \exp\left(\alpha_t \cdot I\left(h_{t(x_j)} \neq y_j\right)\right)\right]} \quad (35)$$

In this manner, sample weights $w_i^{\{(t+1)\}}$ are adaptively reweighted based on how well they separated tumors in PCA space, thus allowing better separation between tumor categories. At every iteration t, the weak classifier h_t has a corresponding weight α_t. If the weak classifier h_t misclassifies the sample i, then the indicator function $I(h_{t(x_i)} \neq y_i)$ will return a value of 1; otherwise, it will return a value of 0. The true label for sample i is represented by y_i, and N is the total number of samples. x_i is input data for the training samples in the iteration that represent t. $h_{t(x_i)}$ gives the prediction made by the weak classifier for the sample j.

III. Model Assessment and Performance Evaluation

An assessment of machine learning models for classification and recognition must take into account several quantitative performance indicators, which are mathematically defined in Eq. (36), Eq. (37), Eq. (38), and Eq. (39) [35], [36], [37], [38], [39], [40]. Accuracy is the principal method of measuring how accurately a classifier performs on a test dataset; it reflects the accuracy with which a classifier classifies data into healthy and unhealthy categories. By using multiple evaluation techniques, the model may be evaluated from many angles, and there will be a better understanding of how the model behaves and how the evaluation process can be made more effective. When evaluating the effectiveness of the model that was trained, the investigators looked at how well the model was able to correctly classify MRI images as healthy and unhealthy. Precision measures the percentage of positive cases correctly identified among all instances identified as positive, while recall measures the number of correctly identified cases of disease relative to the total number of true cases in the dataset. F1 scores combine precision and recall in a way that will result in higher values if both precision and recall are performing well.

$$Accuracy\ (ACC) = \frac{Tp+Tn}{Tp+Tn+Fp+Fn} \quad (36)$$

$$Recall\ (Sensitivity) = \frac{Tp}{Tp+Fn} \quad (37)$$

$$\text{Precision (PPV)} = \frac{Tp}{Tp+Fp} \quad (38)$$

$$F1\_score = \frac{2*Tp}{2*Tp+Fp+Fn} \quad (39)$$

Manuscript received 11 January 2026; Revised 20 March 2026; Accepted 15 April 2026; Available online 24 April 2026
Digital Object Identifier (**DOI**): https://doi.org/10.35882/jeeemi.v8i2.1462

With TP representing the number of true positives (i.e., people with the disease that are correctly identified as having the disease) and TN representing the number of true negatives (the number of people who do not have the disease and are correctly identified as not having the disease), FP represents the number of false positives (i.e., people who do not have a disease but are incorrectly diagnosed with a disease), and FN represents the number of false negatives (i.e., those who have a disease but are not diagnosed).

Table 3. Experimental results of applying MobileNetV3 individually for brain tumor classification.

Algorithm	Accuracy (%)	Precision (%)	Recall (%)	F1-score (%)	Loss	MSE	MAE
MobileNetV3 (without 2D-DWT)	98.72	98.75	98.70	98.72	0.041	0.005	0.007
MobileNetV3 (With 2D-DWT)	99.56	99.58	99.56	99.57	0.026	0.002	0.003

Table 4. Experimental results of the AdaBoost classifier applied to PCA-reduced MobileNetV3 deep features for four-class brain tumor classification.

Feature Extraction	No. of Features	Classifier	Accuracy (%)	Precision (%)	Recall (%)	F1-score (%)	AUC (%)	Dim. R. (%)
2D-DWT + deep Features + PCA	20	AdaBoost	99.94	99.95	99.96	99.94	100	99.96

Table 5. Experimental results of the AdaBoost classifier applied to PCA-reduced MobileNetV3 deep features for four-class brain tumor classification.

Feature Extraction	No. of Features	Classifier	Accuracy (%)	Precision (%)	Recall (%)	F1-score (%)	AUC (%)	Dim. R. (%)
2D-DWT + deep Features + PCA	20	CNN + SoftMax	99.32	99.35	99.30	99.32	100	99.96
2D-DWT + deep Features + PCA	20	SVM	99.41	99.43	99.40	99.41	100	99.96
2D-DWT + deep Features + PCA	20	Random Forest	99.48	99.50	99.47	99.48	100	99.96
2D-DWT + deep Features + PCA	20	KNN	99.37	99.39	99.35	99.37	100	99.96
2D-DWT + deep Features + PCA	20	AdaBoost	99.94	99.95	99.96	99.94	100	99.96

IV. Results

This section details the quantitative assessment of the hybrid method that combines a single-level discrete wavelet transform (2D-DWT), MobileNetV3 for deep feature extraction, and PCA/AdaBoost for classifying multi-class brain tumor MRI.

A. Effect of 2D-DWT Preprocessing on MobileNetV3 Performance

The effects of wavelet-based preprocessing were evaluated first by training MobileNetV3 without 2D-DWT preprocessing using the original MRI images. As shown in Table 3, the baseline configuration achieved an accuracy of 98.72%. With the addition of one-level 2D-DWT preprocessing, classification accuracy increased to 99.56%, showing a 0.84% performance increase. This demonstrates the ability of wavelet-based preprocessing to improve the deep feature extractor's discriminative information. The one-level 2D-DWT decomposition reduces the spatial resolution of input images by about 75% while preserving the relevant tumor characteristics with respect to the input image. The LL sub-band contains anatomical structures with low frequencies and provides global tumor location, while all other sub-bands (LH, HL, & HH) contain high-frequency components of a tumor's boundary and texture irregularities.

B. Performance of the PCA–AdaBoost Hybrid Framework

A 1,024-dimensional feature vector was generated from MobileNetV3 in the deep feature extraction phase. To decrease computational complexity, PCA was used to compress the feature vector into 20 principal components. This dimensionality reduction corresponds to a 99.96% reduction ratio while

Manuscript received 11 January 2026; Revised 20 March 2026; Accepted 15 April 2026; Available online 24 April 2026
Digital Object Identifier (**DOI**): https://doi.org/10.35882/jeeemi.v8i2.1462

Table 6. Computational efficiency comparison.

Model	Feature Dimension	Training Time (s)	Inference Time (ms/image)
MobileNetV3 + SoftMax	1024	182	9.8
MobileNetV3 + SVM	1024	205	11.2
MobileNetV3 + Random Forest	1024	196	10.5
Proposed (MobileNetV3 + PCA + AdaBoost)	20	64	3.9

Table 7. Comparative summary of state-of-the-art methods and the proposed hybrid classification framework for four-class brain-tumor MRI diagnosis.

References	Algorithm	Dataset	Classes	Accuracy (%)
[7]	Ensemble InceptionV3 + Xception	MRI dataset	4 classes	98.5
[8]	VGG16 + ResNet50 + AlexNet Ensemble	MRI dataset	4 classes	99.16
[11]	CE-EEN-B0 + ResGANet + LBP/HOG Fusion	MRI dataset	4 classes	99.11
[12]	LBP + CNN + SHAP	MRI dataset	4 classes	98.9
[13]	SqueezeNet + InceptionV3 TL	MRI dataset	4 classes	99.2
[15]	CNN + LSTM	MRI dataset	4 classes	99.1
Proposed Methodology	1-level-2D-DWT + MobileNetV3	MRI dataset	4 classes	99.56
	1-level-2D-DWT + Deep Features [MobileNetV3] + PCA + AdaBoost	MRI dataset	4 classes	99.94

maintaining over 99.9% of the total variance. The number of retained components was determined using an empirical performance analysis coupled with cumulative explained variance analysis. In summary, the information provided in Table 4 indicates that the overall performance of the hybrid system (2D-DWT, MobileNetV3, PCA, and AdaBoost) will be an approximately 99.94% accurate classification, as well as significantly reduced feature dimensionality. The results using the AdaBoost classifier on PCA-reduced MobileNetV3 deep features extracted after 2D-DWT preprocessing are presented in Table 4. Reducing the dimension of the feature space to 20 principal components yielded excellent results with 99.94% accuracy, 99.95% precision, 99.96% recall, 99.94% F1-score, and 100% area under the receiver operating characteristic curve.

C. Comparison with Other Classifiers on PCA-Reduced Deep Features

To evaluate the performance of different classifiers using PCA-reduced features, Table 5 shows how they compare to each other. Classifiers included in the table are AdaBoost, CNN + SoftMax, SVM, Random Forest, and KNN. All classifiers achieved good performance with an accuracy greater than 99%; however, AdaBoost achieved the highest accuracy with a value of 99.94%.

D. Computational Efficiency

In Table 6, the proposed framework's computation performance will be assessed by comparing the training and inference times for the suggested model with other available models. Reducing the number of features from 1,024 to 20 by using a PCA-reduced feature set will dramatically reduce the computational cost. The proposed framework produced 64 seconds of training time/image and 3.9 milliseconds of inference time/image when compared with the CNN + SoftMax model, which has 182 seconds of training time/image and 9.8 milliseconds of inference time/image. Due to the reduced feature space and improved computational efficiency of the proposed framework, the proposed model is sufficiently accurate for use on real-time clinical applications, even if the available computational resources are limited.

E. Comparison with State-of-the-Art Methods

Table 7 provides a comparison of the proposed hybrid framework with current state-of-the-art techniques, all of which yield comparable or better classification accuracy and lower computational costs compared to traditional approaches. Table 7 proposes obtaining a higher accuracy than other systems that classify four classes of brain tumors in MRIs, all of which obtain accuracies of between 98.5% and 99.2%. The proposed hybrid system achieves 99.56% accuracy using 2D-DWT combined with MobileNetV3, and when it is also combined with PCA and AdaBoost, it obtains an accuracy of 99.94%. Our experimental results

Manuscript received 11 January 2026; Revised 20 March 2026; Accepted 15 April 2026; Available online 24 April 2026
Digital Object Identifier (**DOI**): https://doi.org/10.35882/jeeemi.v8i2.1462

highlight the superior performance of our proposed framework over all current models in terms of both high classification accuracy and lower computational cost, which will allow for greater feasibility in clinical practice.

F. Training Curves, Confusion Matrices, and ROC Analysis

Fig. 6 shows that the training and testing curves converge smoothly without overfitting. The confusion matrices in Fig. 7 indicate reliable classification ability into all four tumor types: glioma, meningioma, pituitary tumor, and no tumor. Almost all samples were accurately classified; the only minor confusion observed was between gliomas and meningiomas. The ROC curve presented in Fig. 8 demonstrates excellent separation between the classes, with an AUC value equal to 1.00.

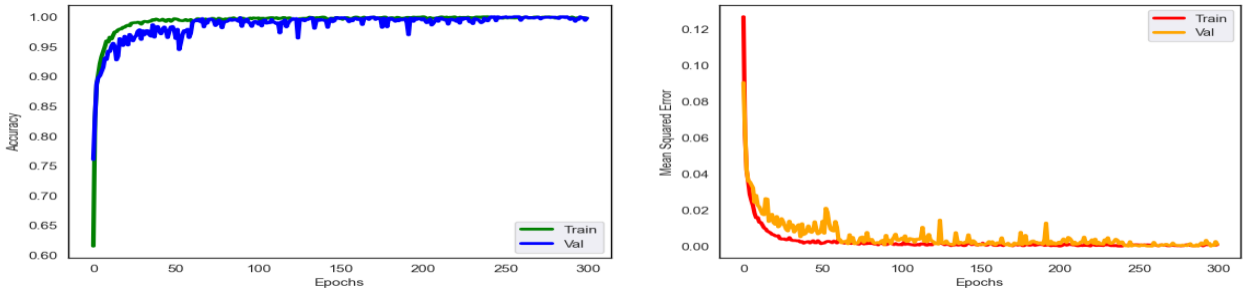

(a) (b)

Fig. 6. MobileNetV3 classifier's training and validation using one-level 2D-DWT (a) Accuracy and (b) MSE.

V. Discussion

The discussion of the present findings is structured around four key aspects: overall performance interpretation, comparison with previous studies, error analysis, and limitations with future implications. The PCA-AdaBoost Hybrid model showed exceptional performance metrics, including 99.94% accuracy, 99.95% precision, 99.96% recall, 99.94% F1 score, and 100% AUC. These metrics vastly exceed those attained with the base MobileNetV3 + 2D-DWT model, which recorded an accuracy of 99.56% (Table 3). PCA has been shown to facilitate model performance efficiencies by reducing the 1,024-dimensional feature space into 20 principal components while maintaining 99.96% of the original data's discriminative capability (Table 4). The 100% AUC (Fig. 8) indicates that the model has demonstrated a remarkable capacity to accurately differentiate between each of the four brain tumor types, and thus the classification capabilities provide a high level of confidence. Using PCA, the dimensionality of the feature vector has been significantly reduced while retaining the highest-order features, which has led to enhanced classification precision, as well as reduced computational costs, making this model well-suited for practical clinical application in real time.

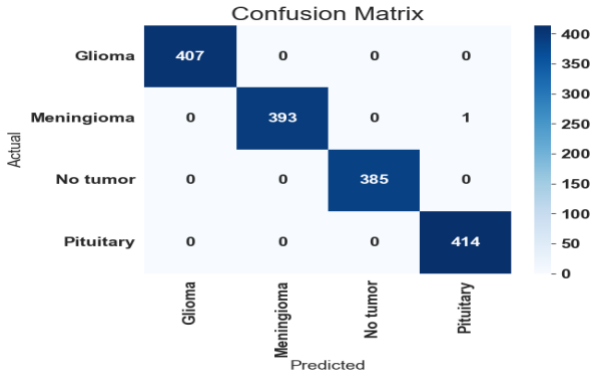

Fig. 7. Confusion matrices for AdaBoost classifier.

In comparison to other recent models, this proposed framework outperforms multiple state-of-the-art techniques. For example, ensemble models such as InceptionV3 and Xception had an accuracy rate between 98.3% and 98.5% (shown in Table 7), while an ensemble of VGG16 plus ResNet50 plus AlexNet had a total accuracy rate of 99.16% (also shown in Table 7). In comparison to these models, the proposed framework achieved a total accuracy of 99.94% (as shown in Table 4) while using significantly less model size and fewer computational resources for deployment. This results in the proposed classification method being more feasible for clinical applications requiring real-time processing. Additionally, Res-BRNet and transfer-learning approaches had accuracies of 98.22% and 99.2%, respectively (shown in Table 7); however, both of these models typically require substantially more computational resources or are not generalizable across different MRI scanner types. The efficiency and practicality of the proposed classification method in real-life clinical settings are clearly demonstrated by this data.

The model was successful, with only a small number of tumors misclassified, particularly gliomas and meningiomas. The similarity of both texture and spectrum between these tumor types likely contributed

Manuscript received 11 January 2026; Revised 20 March 2026; Accepted 15 April 2026; Available online 24 April 2026
Digital Object Identifier (**DOI**): https://doi.org/10.35882/jeeemi.v8i2.1462

to misclassification. The confusion matrix, shown in Fig. 7, is indicative of many misclassifications between these two tumor types. There are several options for addressing this problem, such as expanding the sample types in the dataset or using explainable artificial intelligence (e.g., utilizing Grad-CAM and saliency mapping) to understand the reasons for misclassification. Additionally, continued development of the feature extraction method, with improved spectral-domain features, can improve accuracy and robustness with respect to classifying these tumor types.

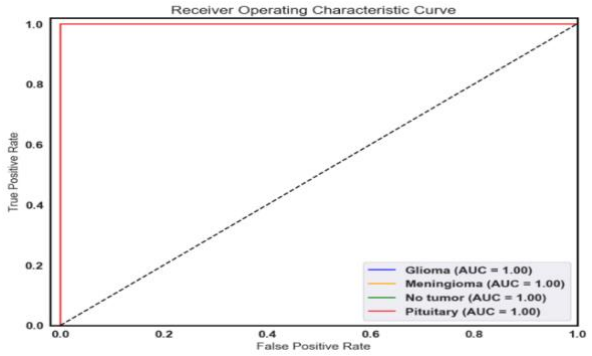

Fig. 8. ROC curve of the AdaBoost ensemble classifier evaluated on the Kaggle dataset using PCA-reduced features (7023 × 20).

The findings presented in this research are encouraging; however, several limitations should be acknowledged. The current work was based on a single public data source (i.e., 7023 images). While this publicly available data has been used by multiple authors in the past, applicability beyond this single dataset is unknown, especially within real-world practice and multi-center studies. Therefore, it is recommended that subsequent research evaluate the proposed algorithm on other datasets as listed in Multi-Center Settings (Table 7), given the missing or absent evaluations of algorithm performance in real-world settings. Since the algorithm has not been validated in actual clinical practice, it would be beneficial for future research to assess the feasibility of diagnosing brain tumors within clinic-based populations and similarly examine the use of real-time data when incorporated into MRI imaging equipment. Furthermore, while the model is currently computationally efficient, future research could explore the integration of more complex architectures or additional data preprocessing techniques to enhance the model's diagnostic capabilities, particularly in handling a broader range of brain tumor types or improving its performance under varying imaging conditions. Such advancements would help extend the applicability of the model to different clinical scenarios and further reduce the computational burden.

VI. Conclusion

The present study focused on the development of a lightweight yet highly accurate framework for multi-class brain tumor classification from medical MRI images. It incorporated multiple resolution spectral and feature representations (e.g., through deep learning), followed by dimensionality reduction, and finally used an ensemble boosting approach to train and evaluate classifiers. In contrast to conventional classification approaches and research that utilize the spectral domain for feature extraction, the proposed system successfully addresses key issues found within those prior methods (e.g., redundancies across deep feature sets, non-inclusion of spectral domain analysis, and high computational requirements of complex deep ensemble models). The combined findings of this research indicate that the hybrid combination of 1-level 2D-DWT + MobileNetV3 + PCA + AdaBoost achieved very high performance with respect to classification (i.e., 99.94% accuracy, 99.95% precision, 99.96% recall, 99.94% F1-score, and 100% AUC), thus exceeding many previously established top-performing classification models. MobileNetV3 by itself provided an outstanding prediction capability with high accuracy (99.56%) on (2D-DWT)-enhanced images; PCA also provided high-dimensionality reduction (i.e., reducing from 1024 to 20 components, a 99.96% reduction) with no negative effect on performance.

This research confirms the existence of a significant enhancement in reliability for any classification application that utilizes a combination of both deep semantic and spectral–textural feature sets. This study further demonstrates that the incomparable framework produced by the authors may become viable for use in resource-constrained or real-time (clinical) settings given the architecture's lightweight nature, low computational burden, and flexibility. Lastly, this study highlights that the framework also reduces the need for complex, large CNN ensemble structures while maintaining excellent diagnostic performance. Future work will focus on extending the model to multi-sequence MRI (e.g., T1, T2, FLAIR), incorporating explainable-AI techniques such as Grad-CAM or SHAP to enhance clinical transparency, evaluating cross-dataset generalization across multi-center data, and exploring non-linear feature-reduction approaches or model-compression techniques to further optimize deployment on embedded medical devices.

References

[1] T. A. Shaikh, S. Hakak, T. Rasool, and M. Wasid, "*Machine Learning and Artificial Intelligence in Healthcare Systems*", *Boca Raton, FL, USA: CRC Press,* 2023, doi:

Manuscript received 11 January 2026; Revised 20 March 2026; Accepted 15 April 2026; Available online 24 April 2026
Digital Object Identifier (**DOI**): https://doi.org/10.35882/jeeemi.v8i2.1462

10.1201/9781003265436.

[2] S. Alsubai, H. U. Khan, A. Alqahtani, M. Sha, S. Abbas, and U. G. Mohammad "Ensemble deep learning for brain tumor detection", *Frontiers in Computational Neuroscience,* Volume 16, pp.1-14, 2022, doi: 10.3389/fncom.2022.1005617.

[3] N. F. Othman and S. W. Kareem, "Brain Tumor Classification Accuracy Using Deep Learning with Real and Synthetic MRI Images," *ZANCO Journal of Pure and Applied Sciences*, pp. 126–149, 2025, doi: https://doi.org/10.21271/ZJPAS.37.4.11.

[4] N. Ullah, A. Javed, A. Alhazmi, S. M. Hasnain, A. Tahir, and R. A. Id, "TumorDetNet : A unified deep learning model for brain tumor detection and classification," *PLOS ONE,* pp. 1–24, 2023, doi: 10.1371/journal.pone.0291200.

[5] Y. Sankararao, and K. Syed, "EBTSC-Enhanced Brain Tumor Segmentation and Classification Using U-Net ++ and Hybrid deep learning Method," *International Journal of Intelligent Engineering and Systems,* Vol. 18, No. 10, pp. 933–948, 2025, doi: 10.22266/ijies2025.1130.59.

[6] B. Ramu, R. B. Tummala, S. Siddamsetti, D. R. S. Victoria, D. Kishore, and N. M. Jyothi, "Accurate Brain Tumor Classification Using GoogLe Net and Extreme Learning Machine (ELM) With Multiple Features," *International Journal of Intelligent Engineering and Systems*, Vol.18, No.11, 2025, doi: 10.22266/ijies2025.1231.22.

[7] A. B. Abdusalomov, M. Mukhiddinov, and T. K. Whangbo, "Brain Tumor Detection Based on Deep Learning Approaches and Magnetic Resonance Imaging," *Cancers*, pp. 1-29, 2023, 15, 4172, https://www.mdpi.com/2072-6694/15/16/4172.

[8] H. M. Al-dabbas and M. S. Mahdi, "Classification of Brain Tumor Diseases Using Data Augmentation and Transfer Learning," *Iraqi Journal of Science,* Vol. 65, No. 4, pp. 2275–2286, 2024, doi: 10.24996/ijs.2024.65.4.41.

[9] M. M. Zahoor, S. H. Khan, T. J. Alahmadi, and T. Alsahfi, A. S. Al Mazroa, H. A. Sakr, S. Alqahtani, A. Albanyan, and B. K. Alshemaimri, "Brain Tumor MRI Classification Using a Novel Deep Residual," *Biomedicines*, pp. 1–19, 2024, doi: 10.3390/biomedicines12071395.

[10] S. Srinivasan, D. Francis, S. K. Mathivanan, H. Rajadurai, B. D. Shivahare, and M. A. Shah, "A hybrid deep CNN model for brain tumor image multi - classification," *BMC Med. Imaging*, pp. 1–21, 2024, doi: 10.1186/s12880-024-01195-7.

[11] R. Khan, S. Taj, Z. U. Khan, S. U. Khan, J. Khan, T. Arshad, and S. Ayouni "High-precision brain tumor classification from MRI images using an advanced hybrid deep learning method with minimal radiation exposure," *J. Radiat. Res. Appl. Sci.*, vol. 18, no. 4, p. 101858, 2025, doi: 10.1016/j.jrras.2025.101858.

[12] A. Rahman, M. Hayat, N. Iqbal, F. K. Alarfaj, S. Alkhalaf, and F. Alturise, "Enhanced MRI brain tumor detection using deep learning in conjunction with explainable AI SHAP based diverse and multi feature analysis," *Scientific Reports,* pp. 1–15, 2025, doi: 10.1038/s41598-025-14901-4.

[13] R. N. Asif, M. T. Naseem, M. Ahmad, T. Mazhar, M. A. Khan, M. A. Khan, A. Al-Rasheed, and H. Hamam, "Brain tumor detection empowered with ensemble deep learning approaches from MRI scan images," *Scientific Reports*, pp. 1–22, 2025, doi: 10.1038/s41598-025-99576-7.

[14] R. F. Jader, S. W. Kareem, and H. Q. Awla, "Ensemble Deep Learning Technique for Detecting MRI Brain Tumor," *Applied Computational Intelligence and Soft Computing,* Vol. 2024, pp. 1-13, 2024, doi: 10.1155/2024/6615468.

[15] M. I. Al-khuzaie and W. A. M. Al-jawher, "Enhancing Medical Image Classification : A Deep Learning Perspective with Multi Wavelet Transform," *Journal port Science Research,* Vol. 6, No. 4, pp. 365–373, 2023, doi: 10.36371/port.2023.4.7.

[16] F. M. J. M. Shamrat, S. Azam, A. Karim, R. Islam, Z. Tasnim, P. Ghosh and F. D. Boer, "LungNet22 : A Fine-Tuned Model for Multiclass Classification and Prediction of Lung Disease Using X-ray Images," and prediction of lung disease using X-ray images", *Journal of Personalized Medicine*, Vol. 12, No. 5, pp. 680, 2022, doi: 10.3390/jpm12050680.

[17] S. N. Nia and F. Y. Shih, "Medical X-Ray Image Enhancement Using Global Contrast-Limited Adaptive Histogram Equalization," *International Journal of Pattern Recognition and Artificial Intelligence*, vol. 38, no. 12, Article 2457010, 2024, doi: 10.1142/S0218001424570106.

[18] M. S. Z. Ahmad, N. A. Ab. Aziz, H. S. Lim, A. K. Ghazali, and A. A. Latiff, "Impact of Image Enhancement Using Contrast-Limited Adaptive Histogram Equalization (CLAHE), Anisotropic Diffusion, and Histogram Equalization on Spine X-Ray Segmentation with U-Net, Mask R-CNN, and Transfer Learning," *Algorithms*, vol. 18, no. 12, Article 796, 2025, doi: 10.3390/a18120796.

[19] M. Mehdizadeh, K. T. Tafti, and P. Soltani,

Manuscript received 11 January 2026; Revised 20 March 2026; Accepted 15 April 2026; Available online 24 April 2026
Digital Object Identifier (**DOI**): https://doi.org/10.35882/jeeemi.v8i2.1462

"Evaluation of Histogram Equalization and Contrast Limited Adaptive Histogram Equalization Effect on Image Quality and Fractal Dimensions of Digital Periapical Radiographs," *Oral Radiology*, vol. 39, no. 2, pp. 418–424, 2023, doi: 10.1007/s11282-022-00654-7.

[20] V. D. Phan, L. C. Chan, A. H. A. Li, Y. T. Chien, and C. V. Nguyen, "Liver cancer prediction in a viral hepatitis cohort: A deep learning approach," *International Journal of Cancer, 147(10), pp. 2871-2878, 2020*, doi: 10.1002/ijc.33245.

[21] B. Sravani and M. S. Kumar, "A Hybrid Deep Ensemble Model for Precise Liver and Tumor Segmentation Using U-Net and W-Net Architectures," *Journal of Electronics, Electromedical Engineering, and Medical Informatics, Vol. 8, No. 2, April 2026, pp: 553-571, 2026,* doi: 10.35882/jeeemi.v8i2.1089.

[22] A. A. Abdullah, A. Aldhahab, and H. M. Al Abboodi, "Deep-Ensemble Learning Models for the Detection and Classification of Eye Diseases Based on Engineering Feature Extraction with Efficientb6 and Densnet169," *Int. J. Intell. Eng. Syst.*, Vol. 17, No. 6, pp. 1001–1022, 2024, doi: 10.22266/ijies2024.1231.75.

[23] S. G. Mallat, "A Theory for Multiresolution Signal Decomposition: The Wavelet Representation",*IEEE Transactions on Pattern Analysis and Machine Intelligence*, vol. 11, no. 7, pp. 674–693, 1989, doi: 10.1109/34.192463.

[24] I. Daubechies, "Orthonormal Bases of Compactly Supported Wavelets," *Communications on Pure and Applied Mathematics*, vol. 41, no. 7, pp. 909–996, 1988, doi: 10.1002/cpa.3160410705.

[25] A. Aldhahab and W. B. Mikhael, "Face Recognition Employing DMWT Followed by FastICA," *Circuits, Syst. Signal Process.*, 2017, doi: 10.1007/s00034-017-0653-z.

[26] A. G. Howard, M. Zhu and B. Chen, "MobileNets: Efficient Convolutional Neural Networks for Mobile Vision Applications," *arXiv preprint* arXiv:1704.04861, 2017.

[27] M. Sandler, A. Howard, M. Zhu, A. Zhmoginov, and L.-C. Chen, "MobileNetV2: Inverted Residuals and Linear Bottlenecks," *Proc. IEEE/CVF Conf. Computer Vision and Pattern Recognition (CVPR)*, pp. 4510–4520, 2018, doi: 10.1109/CVPR.2018.00474.

[28] A. W. Al-funjan, H. M. Al Abboodi, N. A. Hamza, W. M. S. Abedi, and A. H. Abdullah, "A Lightweight Deep Learning-Based Ocular Disease Prediction Model Using Squeeze-and-Excitation Network Architecture with MobileNet Feature Extraction," *Int. J. Intell. Eng. Syst.*, Vol. 17, No. 4, pp. 243–262, 2024, doi: 10.22266/IJIES2024.0831.19.

[29] A. Tharwat, "Principal component analysis - a tutorial," *Int. J. Appl. Pattern Recognit.,* Vol. 3, No. 3, pp. 197-240, 2016.

[30] A. A. Abdullah, A. Aldhahab, and H. M. Al Abboodi, "Eye Disease Classification Based on Hybrid Deep Features with Principal Component Analysis and Blending Ensemble Learning," *Int. J. Intell. Eng. Syst.*, Vol. 18, No. 6, pp. 179–198, 2025, doi: 10.22266/ijies2025.0731.12.

[31] M. Kuhn and K. Johnson, *"Applied Predictive Modeling*," *New York: Springer*, Vol. 26, pp.1-13, 2013, doi: 10.1007/978-1-4614-6849-3.

[32] F. WANG, Z. LI, F. HE, R. WANG, W. YU, and F. NIE, "Feature Learning Viewpoint of Adaboost and a New Algorithm," *IEEE Access*, vol. 7, pp. 149890–149899, 2019, doi: 10.1109/ACCESS.2019.2947359.

[33] Y. Freund and R. E. Schapire, "A Decision-Theoretic Generalization of On-Line Learning and an Application to Boosting," *J. Comput. Syst. Sci.*, Vol. 55, No. 1, pp. 119_139, Aug. 1997, doi: 10.1006/jcss.1997.1504.

[34] P. Wu and H. Zhao, "Some Analysis and Research of the AdaBoost Algorithm," *International Conference on Intelligent Computing and Information Science*. Berlin, Germany: Springer, pp. 1–5, 2011, doi: 10.1007/978-3-642-18129-0_1.

[35] A. A. Abdullah, A. Aldhahab, and H. M. Al Abboodi, "Detection and Classification of Eye Diseases using Hybrid Deep Features with Decision Tree Algorithm," *3rd Int. Conf. Adv. Eng. Sci. Technol. AEST 2024*, vol. 2024, pp. 1–6, 2024, doi: 10.1109/AEST63017.2024.10960200.

[36] S. Bala, K. Arora, R. Jeevitha, R. Chowdhury, P. Kumar, and S. N. C, "A Novel Encoder Decoder Architecture with Vision Transformer for Medical Image Segmentation," *Journal of Electronics, Electromedical Engineering, and Medical Informatics,* Vol. 7, No. 1, pp. 176–186, 2025, doi: 10.35882/jeeemi.v7i1.571.

[37] M. K. Ismael, S. T. Bahar, and A. A. Abdullah, "Harmonic Elimination Method for Permanent Magnet Synchronous Motor Utilizing Active Disturbance Rejection Control," *Proceedings of Engineering and Technology Innovation*, vol. 30, pp. 11–23, 2025, doi: https://doi.org/10.46604/peti.2024.14386.

[38] A. C. Kemila, W. Fawwaz, and A. Maki, "Parameter Optimization of Support Vector

Manuscript received 11 January 2026; Revised 20 March 2026; Accepted 15 April 2026; Available online 24 April 2026
Digital Object Identifier (**DOI**): https://doi.org/10.35882/jeeemi.v8i2.1462

Machine using River Formation Dynamic on Brain Tumor Classification," *Journal of Electronics, Electromedical Engineering, and Medical Informatics,* Vol. 5, No. 3, pp. 177–184, 2023, doi: 10.35882/jeemi.v5i3.312.

[39] A. A. Abdullah, and M. Q. Hatem, "AUDIO TRANSMISSION THROUGH LI-FI," *International Journal of Civil Engineering and Technology*, Vol. 9, No. 7, pp. 853–859, 2018, http://iaeme.com/Home/issue/IJCIET?Volume=9&Issue=7.

[40] M. Gangappa, D. Manju, M. G. Krishnna, M. S. M. Reddy, M.Sathish, S. Shahabaaz, A. Shanthan, and M. Chaitanya, "Quantum-Enhanced Brain Tumor Detection and Progression Prediction Using MRI Imaging," *Journal of Electronics, Electromedical Engineering, and Medical Informatics,* Vol. 7, No. 2, pp. 493–507, 2025. doi: 10.35882/jeeemi.v7i2.720.

Author Biography

Ahmed Aizaldeen Abdullah received his B.Sc. degree in Electrical Engineering from the University of Diyala, Iraq, in 2005, and his M.Sc. degree in Electronic Engineering from the University of Technology – Baghdad, Iraq, in 2014. He earned his Ph.D. in Electrical Engineering from the University of Babylon, College of Engineering, Iraq, in 2026. Dr. Abdullah is currently a faculty member at the Middle Technical University, Electromechanical Techniques Department. His research interests include medical image analysis, machine learning, deep learning, biomedical signal processing, and computer-aided diagnosis. He has published in several Scopus-indexed journals and actively contributes to research on hybrid deep-learning architectures and diagnostic models for healthcare applications. Dr. Abdullah's work focuses on improving the performance and accuracy of diagnostic systems, particularly in medical imaging, through innovative machine learning algorithms and techniques. He can be contacted at: handsome.eng82@mtu.edu.iq

ORCID: https://orcid.org/0000-0002-5231-0540

Hadeel Safaa Hussein received her B.Sc. and M.Sc. degrees in Mechatronics Engineering from the University of Baghdad, Iraq, in 2013 and 2016, respectively. She is currently working as a Lecturer Assistant at Al-Iraqia College of Engineering. Her research interests focus on industrial automation and control systems, with particular emphasis on the application of Programmable Logic Controllers (PLCs) in electromechanical and industrial processes. Her work includes the design and implementation of PLC-based control systems for food production lines, as well as the remote control and monitoring of pneumatic elevator systems. Her research aims to enhance the efficiency, reliability, and safety of industrial automation systems.

Email: hadeel.s.hussein@aliraqia.edu.iq

ORCID: https://orcid.org/0009-0000-8295-3910

Professor Laith Ali Abdul-Rahaim (Member, IEEE) was born in Babylon, Iraq, in 1972. He earned his B.Sc. degree in Electronics and Communications Engineering from the University of Baghdad in 1995. He then completed his M.Sc. and Ph.D. degrees in Electronics and Communication Engineering at the University of Technology, Iraq, in 2001 and 2007, respectively. Professor Laith has been a faculty member at the University of Babylon, Iraq, since 2003, where he currently serves as the Dean of the College of Engineering. His research interests span various areas of telecommunications and signal processing, including MC-CDMA, OFDM, MIMO-OFDM, CDMA, space–time coding, modulation techniques, and image processing. He has published extensively in these fields and has contributed to advancing communication technologies.

Email: drlaithanzy@uobabylon.edu.iq

ORCID: https://orcid.org/0000-0001-8064-4401

Manuscript received 11 January 2026; Revised 20 March 2026; Accepted 15 April 2026; Available online 24 April 2026
Digital Object Identifier (**DOI**): https://doi.org/10.35882/jeeemi.v8i2.1462